Probability density functions of hydraulic head and velocity in three-dimensional heterogeneous porous media

Wolfgang Nowak,[1,2] Ronnie L. Schwede,[3] Olaf A. Cirpka,[3] and Insa Neuweiler[1,4]

[1] In this study, we assess probability density functions of hydraulic heads and specific discharges in three-dimensional bounded heterogeneous porous media by Monte Carlo (MC) simulation. We discuss their empirical shapes and demonstrate that the intuitive use of obvious information on boundedness leads to parametric distribution functions, which fit surprisingly well. On the basis of statistical moments of hydraulic heads and velocities up to fourth order, we discuss the spatial dependence of the empirical distributions and their dependence on the variance of log conductivity. Comparison of the first and second central moment to the results from classical numerical first-order second-moment (FOSM) analysis reveals that FOSM predicts these moments surprisingly close for hydraulic heads. On the basis of this fact, we demonstrate that fitting the chosen parametric distributions for hydraulic heads to FOSM moments is promising for the sake of estimating exceedance probabilities. Our MC scenarios vary in variance of log conductivity (0.125 to 5.0), in the type of multivariate dependence, in correlation scale and types of boundary conditions. Our study illustrates that in contrast to the common assumption, FOSM is a reasonable choice for evaluating multivariate and univariate moments for heads, if used in conjunction with additional information on distribution shapes. In the absence of utilizable additional information, we demonstrate that second-moment methods are mostly inadequate for assessing distributions accurately. Significant deviations from Gaussian distributions occurred for discharge components even at a variance of log conductivity as low as 0.125, and we found that the distributions of transverse discharge components are extremely fat-tailed. The observed non-Gaussianity questions the results of approximate approaches in solute flux and dispersion studies where velocity fields are assumed to be multi-Gaussian and then directly represented by or generated from their covariances. The main implication is to apply more accurate schemes such as exact non-local methods, extensive MC or higher-order stochastic Galerkin approaches, and to include higher-order moments, at least if no additional assumptions on the shape of distributions are available or justifiable.

1. Introduction

[2] Most stochastic analyses of flow in heterogeneous porous media evaluate first and second stochastic moments of flow-related variables and mainly differ in the order of approximation or level of accuracy. First-order second-moment analysis (FOSM) is a conceptually simple and computationally quick way to approximate mean values and variances of dependent quantities in stochastic differential equations such as the stochastic flow equation. One particular strength of numerically based FOSM methods is their ability to handle arbitrary domain geometries, arbitrary boundary conditions and arbitrary trends in the conductivity field [e.g., *Kitanidis*, 1997, pp. 196]. When cleverly exploiting problem geometries, using the adjoint-state sensitivity method [*Sun*, 1994] and FFT-based methods for handling stationary or intrinsic covariance functions [e.g., *Nowak et al.*, 2003; *Cirpka and Nowak*, 2004], FOSM methods outrun most other numerical methods while being conceptually simple. This holds especially when stochastic moments at only a few locations are required.

[3] The mathematics quickly become quite intractable beyond first-order second-moment analysis. Still, there is a list of studies that account for higher-order effects in the stochastic flow equation when assessing first and second moments. For an overview of analytical perturbation and expansion methods, we refer to the books of *Rubin* [2003] and *Zhang* [2002].

[4] The restriction to bounded domains with arbitrary boundary conditions reduces the number of available ana-

[1] Institute of Hydraulic Engineering (LH2), Universität Stuttgart, Stuttgart, Germany.
[2] Civil and Environmental Engineering, University of California, Berkeley, California, USA.
[3] Water Resources and Drinking Water, Swiss Federal Institute of Aquatic Science and Technology (Eawag), Dübendorf, Switzerland.
[4] Institute for Fluid Mechanics, Leibniz Universität Hannover, Hannover, Germany.

lytical results [e.g., *Paleologos et al.*, 1996] for the stochastic flow problem. Available numerical methods include exact non-local formalisms for solving the stochastic moment equations [e.g., *Guadagnini and Neuman*, 1999], higher-order perturbation approaches based on polynomial expansion [e.g., *Chaudhuri and Sekhar*, 2005], combinations of polynomial expansions with Karhunen-Loeve expansions of the conductivity field [e.g., *Zhang and Lu*, 2004; *Lu and Zhang*, 2004] or stochastic Galerkin procedures invoking the concept of polynomial chaos or the Askey scheme together with the Karhunen-Loeve expansion [e.g., *Ghanem*, 1998; *Xiu and Karniadakis*, 2002; *Matthies and Keese*, 2005]. Most of these methods, with their polynomial expansions truncated at first order and with no further significant approximations in the representation of the random field (no significant truncation of the Karhunen-Loeve expansion) converge toward traditional FOSM at a similar computational complexity and with comparable results.

[5] In spite of the large range of numerical methods, studies that deal with moments of third order or higher are hard to find. As a matter of fact, the authors are not aware of any analytical expressions for skewness and kurtosis of flow variables in the literature. Only in a very recent study, *Li and Zhang* [2007] discuss the reconstruction of probability density functions from higher-order stochastic expansion approaches by sampling methods.

[6] In absence of higher-order moments and better knowledge, the most common explicit or implicit assumption that accompanies second-moment analysis is that the analyzed quantities obey univariate or multivariate normal distributions, which constitutes a maximum-entropy assumption on the distribution shape. For example, *Cvetkovic et al.* [1992] and *Dentz et al.* [2002, 2003] perform Monte Carlo (MC) studies with velocity fields directly generated from their first-order covariances in order to examine the large-time limits of ensemble dispersion, local-scale dispersion and other transport-related quantities without having to solve the flow equation repeatedly.

[7] Mostly, however, log conductivity is assumed to be Gaussian, so that the independent parameter used in the flow equation is lognormal instead of normal to begin with. Although the groundwater flow equation reveals a linear relationship between heads and source terms, the relationship between log conductivity and heads is well known to be non-linear. This results in non-Gaussian statistical distributions of both hydraulic heads or velocities, especially for cases with a high variance of log conductivity: For example, the increasing skewness and kurtosis of velocity components with increasing field variance of log conductivity has been demonstrated by *Englert et al.* [2006]. We suspect that ignorance of higher-order moments and/or of the actual distribution shape may have severe consequences for the accuracy of macro-transport theory, stochastic system analyses or design tasks under uncertainty.

[8] For example, the evaluation of exceedance probabilities in risk assessment and stochastic design requires assumptions or knowledge of the actual shape of distributions. Assuming the normal distribution to obtain confidence intervals from second moments may be highly inaccurate if the actual distribution differs significantly from the normal. In some cases, however, workarounds may be found. To give an example, *Cirpka et al.* [2004] deal with the stochastic design of funnel and gate systems. They argued that mass flux capture efficiencies of funnel and gate systems are designed close to their physical maximum of 100%, hence have asymmetric bounds and thus are heavily tailed toward smaller values, following an otherwise unknown distribution shape. To evade this problem, they hypothesized that stream function values at the plume and at gate edges follow a quasi-Gaussian distribution since they are sufficiently far from any physical bounds. Then, they used their statistics in their design procedure. Unfortunately, such workarounds to find adequate pseudo Gaussian variables with almost-linear relations to the uncertain parameters are available in very few cases only.

[9] Amid general higher-order effects that cause non-Gaussian behavior of dependent quantities, there are at least two distinct ones that affect the shape of distributions: First, the physical requirement of non-negativity constitutes a one-sided bound for some dependent quantities. The specific discharge, for example, is practically non-negative in the direction of mean flow in all but the unlikely case that high-contrast structures in conductivity lead to a local reversal of flow. Second, boundary conditions may cause the range of admissible values to be bounded. For example, hydraulic heads between two Dirichlet boundaries in absence of recharge and discharge are bounded to the interval between the fixed-head values at the boundaries. A comparable behavior is that solute concentrations are bounded between zero and some initial or fixed concentration value, as has been demonstrated by *Caroni and Fiorotto* [2005].

[10] We expect the distribution shapes of flow-related quantities to depend on the vicinity to a restricting boundary, and hence on space in general. This change in distribution shape is accompanied by well-studied effects such as the dependence of variance on the distance to the boundaries in bounded domains [e.g., *Paleologos et al.*, 1996; *Zhang and Winter*, 1999]. In order to investigate these effects and the distance to Gaussianity in this study, we evaluate empirical probability density functions for all quantities of interest. We do this on a dense grid of observation locations in order to visualize and quantify the spatial dependence of distribution shapes. Fitting parametric distributions that honor boundedness to these empirical distributions is quite tempting, and we demonstrate how close an intuitive choice of parametric distributions can get to the empirical distributions. The spatial change of distribution shapes is also visualized by plotting empirical higher-order stochastic moments in space.

[11] *Englert et al.* [2006] provide an excellent overview over the large number of recent three-dimensional Monte Carlo studies on stochastic flow, which we summarized here in brief. The Monte Carlos studies by *Dykaar and Kitanidis* [1992] and *Englert et al.* [2006] use low numbers of realizations ($n_r \leq 10$), but resolve their domains finely with more than 10^7 elements, so that they can obtain stochastic moments by spatial averaging of statistics through invoking the principle of ergodicity. Other authors such as *Naff et al.* [1998] or *Neuman et al.* [1992] use higher numbers of realizations with $n_r = 900$ and $n_r = 500$, respectively.

[12] For the purpose of evaluating space-dependent empirical probability density functions, however, a much higher number of realizations is required. Most of all,

simple spatial averaging is not applicable since it would destroy the desired spatial information. In our study, we use $n_r = 25,000$ realizations. For an adequate spatial resolution at bearable computational costs, we choose a spatial resolution by $\approx 2.5 \times 10^5$ elements in each realization. In order to improve the convergence of our MC results, we define the horizontal transverse direction to be periodic. In this case, all statistics are invariant with respect to translation in y, and we apply averaging of statistics along that direction without destroying spatial information along the other directions.

[13] Besides assessing the spatial dependence of distribution shapes and the distance to Gaussianity, we also assess how good first-order second-moment (FOSM) approximations to the mean and variance of distributions are, compared to empirical moments from Monte Carlo analysis (MC). We will demonstrate that, in some cases, these two moments are approximated sufficiently close by FOSM techniques. Subsequently, we hypothesize parametric distributions that honor external knowledge on boundedness and match them with the FOSM-based moments to again test the closeness of the resulting fit.

[14] The analysis of empirical distributions, fitting parametric distributions and matching with FOSM-based moments is performed for a set of Monte Carlo scenarios which differ in the variance of log conductivity. We repeat the same analysis for a second set of Monte Carlo scenarios which focuses on the influence of spatially connected extreme values, using the transformed fields introduced by *Zinn and Harvey* [2003]. Additional investigations deal with different boundary conditions, and with more or less ergodic domains. All of these scenarios use a constant anisotropy ratio of the random conductivity fields.

2. Methods

2.1. Simulation of Flow

[15] Specific discharge $\mathbf{q}$ $[LT^{-1}] = (q_x, q_y, q_z)$ in a porous medium is defined by Darcy's law:

$$\mathbf{q} = -K\nabla\phi \qquad (1)$$

in which K $[LT^{-1}]$ is the hydraulic conductivity, here assumed isotropic on the local scale, and ϕ $[L]$ is the hydraulic head. Total discharge is denoted by Q_x $[L^3 T^{-1}]$. Under steady-state conditions without internal sources and sinks, mass conservation yields the steady-state groundwater flow equation:

$$\nabla \cdot (K\nabla\phi) = 0 \quad \text{in } \Omega$$

$$\mathbf{n} \cdot (K\nabla\phi) = \hat{q} \quad \text{on } \partial\Omega_{no} \qquad (2)$$

$$\phi = \hat{\phi} \quad \text{on } \partial\Omega_D$$

with Ω and $\partial\Omega = \partial\Omega_{no} \cup \partial\Omega_D$ denoting the domain and its boundary, which we have restricted to Dirichlet and no-flow conditions for the greatest part of our simulations. $\hat{\phi}$ is a prescribed head function, $\hat{q}$ is a prescribed flux function (set to zero in most simulations) and $\mathbf{n}$ is the unit normal outward vector. We implemented a vectorized Standard Galerkin Finite Element Method (FEM) code specialized to regular grids and a tailored geometric multigrid PCG solver [e.g., *Press et al.*, 1992] in MATLAB (R2006b) to efficiently discretize and solve the flow equation (equation 2) in $\mathcal{O}(n_g \log n_g)$, n_g being the number of grid nodes. The FEM code used cuboidal elements with trilinear interpolation for ϕ and element-wise constant values of K. FEM-consistent velocities are non-conforming across element edges. Preferring consistent velocities over non-conforming techniques (such as discussed by *Cordes and Kinzelbach* [1992]), we restricted our stochastic analyses to consistently evaluated specific discharge components at element centers.

[16] Our flow domain is three-dimensional, sized $L_x \times L_y \times L_z = 100$ m $\times$ 50 m $\times$ 25 m. We chose periodic boundary conditions along the y-direction (for reasons explained in section 2.3), while the z-direction boundaries were assigned no-flow conditions. The x-direction, being our direction of mean flow, was assigned to have Dirichlet boundaries with a head difference of $\Delta\phi = 1$ m, satisfying the required periodicity in y-direction. The domain was discretized by $80 \times 64 \times 48$ elements ($n_e = 245,760$) with $n_g = 257,985$ nodes to fit the coarsening procedure of our solver. One flow simulation took an average of 8 multigrid PCG iteration steps and 26 seconds with a relative error norm $L_2 = 10^{-10}$, running on a contemporary desktop computer.

2.2. Generation of Random Log Conductivity Fields

[17] We consider second-order stationary fields of $Y = \ln K$ with known mean $\bar{Y}$. The fields are multivariate Gaussian with anisotropic exponential or spherical covariance functions:

$$C_{YY,\exp}(h) = \sigma_Y^2 \cdot \exp(-h) \qquad (3)$$

$$C_{YY,sph}(h) = \begin{cases} \sigma_Y^2 \cdot \left(1 - \dfrac{3}{2}\dfrac{h}{h_r} - \dfrac{1}{2}\dfrac{h^3}{h_r^3}\right) & \text{for } 0 \le h \le h_r \\ 0 & \text{for } h > h_r \end{cases} \qquad (4)$$

where σ_Y^2 is the variance, $h_r[-]$ is the spherical range parameter, and $h[-]$ is the (anisotropic) effective separation distance scaled by the correlation length scales $\lambda_i[L]$, $i = 1, 2, 3$:

$$h = \sqrt{\sum_{i=1}^{3} \left(\sqrt{h_i^2/\lambda_i^2 + d^2} - d\right)^2} \qquad (5)$$

Here $d[-]$ is a microscale (smoothing) parameter relative to λ_i [*Kitanidis*, 1997], and h_i is the separation vector component in direction i. Because conductivity is not defined on arbitrarily small scales, it is justified to define it smooth on the local scale, like the moving average of a noisy sub-scale process. The microscale parameter d acts like a microscale filter on the generated random fields. It also reduces fine-scale stochastic noise in all dependent quantities, improving the convergence of our MC results.

[18] A second type of random fields is obtained from multivariate Gaussian fields Y by the bijective transformation:

$$Y_{(\pm)} = \bar{Y} \pm \sqrt{2}\,\mathrm{erf}^{-1}\left(2\mathrm{erf}\left(\frac{|Y'|}{\sqrt{2}}\right) - 1\right) \qquad (6)$$

Table 1. Definition of Monte Carlo Scenarios[a]

No.	σ_Y^2	$(\lambda_x, \lambda_y, \lambda_z)$ [m]	Miscellaneous
1	0.125	(10, 20, 5)	-
2	0.25	(10, 20, 5)	-
3	0.5	(10, 20, 5)	-
4	1.0	(10, 20, 5)	-
5	1.75	(10, 20, 5)	-
6	2.5	(10, 20, 5)	-
7	3.75	(10, 20, 5)	-
8	5.0	(10, 20, 5)	-
9	2.5	$(10, 20, 5) \cdot \frac{5}{8}$	$Y_{(+)}$
10	2.5	$(10, 20, 5) \cdot \frac{5}{8}$	$Y_{(-)}$
11	2.5	(10, 20, 5)	Neumann BC
12	2.5	(10, 20, 5)	linear $C(h)$ (fractal)
13	2.5	$(10, 20, 5) \cdot \frac{1}{2}$	(closer to ergodicity)

   [a]Unless stated otherwise, domain size is $\mathbf{L}[m] = (100 \times 50 \times 25)$, random field type is multi-Gaussian, covariance model is exponential, using the specified field variance σ_Y^2 and correlation length scales λ_x, λ_x and λ_z. $Y_{(+)}$ and $Y_{(-)}$ indicate transformed fields according to equation (6) [*Zinn and Harvey*, 2003]. The scale factor of 5/8 maintains the integral scale of the transformed fields. In all cases, the microscale parameter is $d = 0.25$, the discretization is $n_e = [80 \times 64 \times 48]$ and the number of realizations is $n_r = 25,000$.

as described by *Zinn and Harvey* [2003], in which $Y' = Y - \bar{Y}$ and $|\cdot|$ is the absolute value. This transformation maintains univariate Gaussianity, but installs a more complex multivariate structure: $Y_{(+)}$ has inclusions of high values in a connected low-value background and $Y_{(-)}$ has low-value inclusions in a connected high-value background. Prior to transformation, Y has low and high-value inclusions in a connected mean-value background. The transformation also changes the correlation structure and therefore requires the correlation length to be multiplied by a factor of 5/8 to install the same integral scale of the transformed fields as in the base case scenarios. All random conductivity fields were generated to be periodic along the y-direction, matching with the periodic boundary conditions of the flow equation. We implemented the FFT-based fast and exact random field generator by *Dietrich and Newsam* [1993], taking less than one second per realization on our computer.

2.3. Monte Carlo Analysis

[19] Our MC scenarios differ in variance of log conductivity within the range of $0.125 \leq \sigma_Y^2 \leq 5$, in the type of multivariate dependence, correlation scale and boundary conditions. A complete list of scenarios and statistical properties of the corresponding random conductivity fields is shown in Table 1. The correlation length scales are deliberately chosen to be relatively large compared to the domain size in order to observe well-pronounced boundary effects over large parts of the computational domain. Scenario 13 served as a more ergodic case for comparison.

[20] We consider the following random variables: log conductivity $Y = \ln K$, hydraulic head ϕ, specific discharge components q_x, q_y and q_z, and total discharge Q_x. In our analysis, we normalized these quantities:

$$\phi^* = \phi / \Delta\phi$$

$$q_i^* = q_i / (K_e I_0), \quad \text{for } i = x, y, z \qquad (7)$$

$$Q_x^* = Q_x / (K_e I_0 A)$$

where $\Delta\phi$ is the head difference between the Dirichlet boundaries. For normalization, we used the effective hydraulic conductivity for isotropic media, $K_e = \exp(\bar{Y} + \sigma_Y^2/6)$ [e.g., *Gelhar and Axness*, 1983; *King*, 1987], the mean hydraulic gradient $I_0 = \Delta\phi / L_x$, and the cross-sectional Area A. After normalization, Q_x^* should be unity for an ergodic and isotropic domain. We are aware that scaling with $\exp(\sigma_Y^2/6)$ is valid for statistically isotropic and ergodic media only [e.g., *Rubin*, 2003], but we still use it in our anisotropic non-ergodic case as approximate scaling. The numerical value of K_e in each realization is the isotropic ergodic theoretical value for K_e corrected by the respective value of Q_x^*, and the empirical ensemble expectation of K_e is the theoretical K_e times the empirical ensemble mean of Q_x^*.

[21] For each random variable $s = \{Y, \phi^*, q_x^*, q_y^*, q_z^*, Q_x^*\}$ we recorded finely resolved histograms with relative frequencies f_s:

$$f_s(\mathbf{x}, C_c) = \frac{1}{n_r} \sum_{r=1}^{n_r} I(L_c < s_r(\mathbf{x}) \leq U_c) \qquad (8)$$

sampled on a $21 \times 17 \times 13$ grid of locations $\mathbf{x}$ (every fourth node in each direction) with bin index c, bin center C_c, lower and upper bin limits L_c and U_c, constant bin width and an auto-adaptive number of classes initially set to $n_c = 200$. $I(\cdot)$ is an indicator function that returns a value of unity if the condition specified inside the brackets is true, and zero otherwise. Of course, Q_x^* has no space dependence. In order to better resolve, visualize and discuss spatial trends in the behavior of space variables, we assessed the following empirical statistics on the entire finite element grid:

$$\mu_s(\mathbf{x}) = \frac{1}{n_r} \sum_{r=1}^{n_r} s_r(\mathbf{x}) \qquad (9)$$

$$\sigma_s^2(\mathbf{x}) = \frac{1}{(n_r - 1)} \sum_{r=1}^{n_r} (s_r(\mathbf{x}) - \mu_s(\mathbf{x}))^2 \qquad (10)$$

$$\gamma_s(\mathbf{x}) = \frac{n_r}{(n_r - 1)(n_r - 2)} \sum_{r=1}^{n_r} \left(\frac{s_r(\mathbf{x}) - \mu_s(\mathbf{x})}{\sigma_s(\mathbf{x})} \right)^3 \qquad (11)$$

$$\eta_s(\mathbf{x}) = \frac{n_r(n_r + 1)}{(n_r - 1)(n_r - 2)(n_r - 3)} \sum_{r=1}^{n_r} \left(\frac{s_r(\mathbf{x}) - \mu_s(\mathbf{x})}{\sigma_s(\mathbf{x})} \right)^4$$
$$- 3 \frac{(n_r - 1)^2}{(n_r - 2)(n_r - 3)} \qquad (12)$$

where μ_s, σ_s^2, γ_s and η_s are estimators of the ensemble mean, variance, skewness and kurtosis, respectively, $\mathbf{x}$ is the location, and μ_s, σ_s^2 are unbiased. The definition of kurtosis used here is also known as kurtosis excess, where the Gaussian distribution has a kurtosis of zero.

[22] The effect of periodicity in y-direction is that all statistics are invariant with respect to y, so all statistics can be averaged along the y-axis without loss of spatial information. This significantly improves the efficiency and

Table 2. Selected Two-Parameter and Three-Parameter Probability Density Functions $p(s)$, Their Mean Values μ_s and Their Variances $\sigma_s^2 B(\cdot)$ is the Beta-Function and $\Gamma(\cdot)$ is the Gamma-Function [e.g., *Evans et al.*, 2000]

Name	pdf $p(s)$	Mean μ_s	Higher Moments (σ_s^2, η_s)
Gaussian	$\dfrac{1}{\sqrt{2\pi b^2}} \cdot \exp\left(-\dfrac{(s-a)^2}{2b^2}\right)$	a	$\sigma_s^2 = b_s^2$
Lognormal	$\dfrac{1}{s \cdot \sqrt{2\pi b^2}} \cdot \exp\left(-\dfrac{1}{2}\dfrac{(\ln s - a)^2}{b^2}\right)$	$\exp\left(a + \dfrac{b^2}{2}\right)$	$\sigma_s^2 = \dfrac{\exp(b^2) - 1}{\exp(2a - b^2)}$
Beta	$\dfrac{1}{B(a,b)} \cdot s^{a-1}(1-s)^{b-1}$	$\dfrac{a}{a+b}$	$\sigma_s^2 = \dfrac{ab}{(a+b)^2(a+b+1)}$
Laplace	$\dfrac{1}{2b} \cdot \exp\left(-\dfrac{|s-a|}{b}\right)$	a	$\sigma_s^2 = 2b^2$
Exponential power	$\dfrac{1}{2b\Gamma(1+1/k)} \cdot \exp\left(-\dfrac{|s-a|^k}{b^k}\right)$	a	$\sigma_s^2 = \dfrac{b^2}{3}\dfrac{\Gamma(1+3/k)}{\Gamma(1+1/k)}$ $\eta_s = \dfrac{9}{5}\dfrac{\Gamma(1+5/k)\Gamma(1+1/k)}{\Gamma^2(1+3/k)}$

accuracy of our analysis. We perform this averaging in a post-processing step so that we can compare the moments before and after averaging. The Monte Carlo code was implemented in MATLAB and directly coupled to the random field generator and the FEM modules to obtain all statistics on-the-fly. The total average CPU-time per realization was at about 55 seconds.

[23] For a small number of reference locations, we kept all simulation data to check convergence using jackknife methods [e.g. *Wonnacott and Wonnacott*, 1990]. For relative frequencies we assume the binomial distribution with $n = n_r$ and $p = f_s/n_r$ for each bin, which is asymptotically exact for large n_c and large n_r. Hence histogram counters have a coefficient of variation of $CV = (n_r f_s)^{-1/2}$, e.g., $CV = 0.02$ for a histogram bin with relative frequency of $f_s = 10\%$. The statistics of Y were used to assure the exactness of the random field generator. Further aspects of convergence are discussed at the end of section 3.1.

2.4. First-Order Second-Moment Analysis

[24] For comparison to the stochastic moments from MC analysis, we perform first-order second-moment analysis to yield approximate mean values, variances and covariances of all dependent random variables s. To evaluate the expected value of all dependent variables, we use the zero-order approximation obtained by solving the flow equation with the homogeneous value of $K_g = \exp(\bar{Y})$. For variances and covariances, we linearized the flow equation about K_g using a Jacobian matrix $\mathbf{H}_s$ derived from adjoint-state sensitivities (see Appendix A):

$$\mathbf{H}_s : H_{jk} = \frac{\partial s(\mathbf{x}_j)}{\partial Y(\mathbf{x}_k)}, \quad k = 1, \ldots, n_e \quad (13)$$

The advantage of adjoint-state sensitivities over direct numerical differentiation is that only one differential equation (which is formally identical to the flow equation in our case) needs to be solved to obtain $\mathbf{H}_s$ for one dependent variable at one location of $\mathbf{x}_j$, regardless of the number of elements n_e.

[25] In this study, unlike in practical applications, we wish to evaluate the moments of the state variables at all locations $\mathbf{x}_j$ in the domain. Exploiting symmetry of the

problem and periodicity in y-direction, only 1025 positions $\mathbf{x}_j$ were required to cover the sensitivities of all values of one variable with respect to all values of $\ln K$ (the lower left 41×25 quarter of the x, z plane at an arbitrary y-position). With only one sensitivity of Q_x with respect to Y, this totaled 5126 adjoint-state problems for all dependent variables (1025 for ϕ, q_x, q_y and q_z each, plus one for Q_x).

[26] Given the sensitivities $\mathbf{H}$ and an auto-covariance matrix $\mathbf{C}_{YY}$ of $Y = \ln K$ evaluated according to equations (3) or (4), linear error propagation yields the cross-covariances between Y and dependent variables s and auto-covariances of dependent variables s:

$$\mathbf{C}_{Ys} = \mathbf{C}_{YY}\mathbf{H}^T \quad (14)$$

$$\mathbf{C}_{ss} = \mathbf{H}\mathbf{C}_{YY}\mathbf{H}^T \quad (15)$$

The space-dependent variance of a dependent variable s can directly be read from the diagonal of $\mathbf{C}_{ss}$. In order to efficiently evaluate equations (14) and (15), we use fast and exact spectral methods for multiplication of covariance matrices as described by *Nowak et al.* [2003].

2.5. Fitting Parametric Distributions

[27] We restrict most of our analyses of random flow variables to two-parameter probability distributions, since their parameters could be directly inferred from first and second stochastic moments, if desired. In absence of any other information than first and second moments, the maximum-entropy univariate probability density function (pdf) that satisfies these moments is the Gaussian. However, physical properties of an observed system may imply boundedness of a stochastic variable, suggesting to apply other parametric distributions. A simple two-parameter distribution that honors non-negativity is the lognormal distribution, and a two-parameter distribution that honors two-sided boundedness is the beta-distribution with support of [0; 1]. The corresponding probability density functions, mean values and variances are provided in Table 2. For properties of these distributions, see article by *Evans et al.* [2000]. For some quantities, we will also make use of the family of exponential power distributions, which includes the Laplace and the Gaussian distributions as special cases for $k = 1$ and
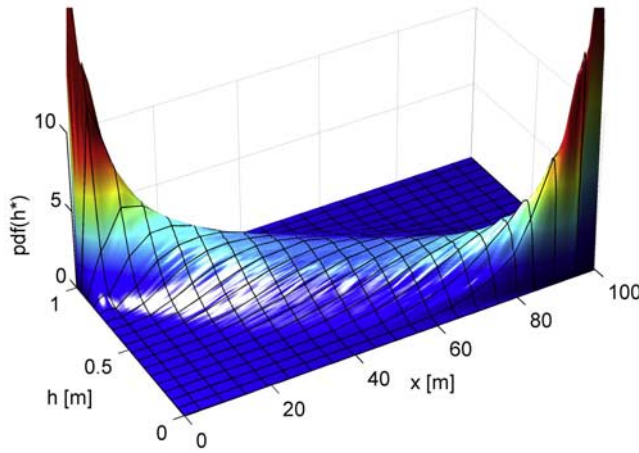
Figure 1. Evolution of the empirical probability density of normalized hydraulic head $\phi^* = \phi/\Delta\phi$ on the centerline along the main direction of flow for scenario 6 ($\sigma_Y^2 = 2.5$).

$k = 2$, respectively. The corresponding moments have been taken from integral tables [*Abramowitz and Stegun*, 1972].

[28] In order to fit these parametric distributions $p_s(a, b, k)$ (k is only required for the exponential distribution family) to the histograms obtained from the MC analysis, we used maximum-likelihood estimation (MLE) [e.g., *Law and Kelton*, 1992]. The MLE parameters (a, b, k) of a chosen parametric distribution maximize the log likelihood $\log L$ for observing an empirical histogram when sampling from the respective parametric distribution:

$$\log L(f_s, C_c, a, b, k)$$
$$= \sum_{c=1}^{n_c} f_c n_r \log(p(C_c, a, b, k)) \rightarrow \max \qquad (16)$$

We fitted the same parametric distributions p_s to the moments obtained from our FOSM or MC analysis by matching the moments (MM). For this purpose, we rearranged the expressions for mean and variance provided in Table 2 for the parameters (a, b, k).

[29] The quality of fitting between parametric distributions p_s and empirical curves f_s from our histogram analysis was assessed using a one-sided χ^2 hypothesis test on a $\alpha = 5\%$ significance level based on the test statistic

$$\chi_{test}^2 = \sum_{c=1}^{n_c} \frac{(\Delta P_s(C_c) - f_s(C_c))^2}{\sigma_{err}^2} \qquad (17)$$

where ΔP_s is the portion of the parametric distribution falling into the respective histogram bin. Because we do not expect our empirical choice of parametric distributions to be exact, we set

$$\sigma_{err}^2 = \Delta P_s(C_c) + \varepsilon_{err} \cdot \Delta P_s^2(C_c) \qquad (18)$$

The first term corresponds to the standard χ^2-test for distribution fitting. Without further modification, given the high number of realizations used in our analyses, the histograms would have to almost exactly resemble the tested parametric shapes in order to pass the test. Hence we use the additional relative error ε_{err} in order to allow a slight model misfit between parametric and empirical curves, here

subjectively chosen to be $\varepsilon_{err} = 0.01$. A fit is rejected if $\chi_{test}^2 > \chi_{\eta,1-\alpha}^2$. $\chi_{\eta,1-\alpha}^2$ is the $1 - \alpha$ quantile of the χ^2-distribution with $\eta = n_c - n_p$ degrees of freedom, n_p is the number of fitted parameters in p_s and n_c is the number of classes.

[30] Later we will see that we encounter many fat-tailed distributions (i.e., with a kurtosis greater than the Gaussian, $\eta > 0$), so we are concerned about the quality of fit in the tails. While the χ^2-test is good to check the quality of fit between histogram and parametric distributions, it would not detect insignificant but systematic mis-estimation of distribution tails. Insignificant but systematic mis-estimation may sum up in cumulative distribution functions to significant mismatches of the far tails. To test for this type of misfit, we additionally apply the Kolmogorov-Smirnov (KS) test, where the absolute deviation between cumulative frequencies and the cumulative distribution function is assessed:

$$KS_{test} = \sup(|F_s(s) - P_s(s)| : s \in \mathcal{R}) \qquad (19)$$

Here F_s are the cumulative relative histogram frequencies from our MC analysis and P_s are the corresponding cumulative probabilities of the fitted parametric distributions. The critical value of the test statistic for $n_r > 35$ is given by

$$KS_{crit} = \sqrt{-\frac{1}{2n_r} \ln\left(\frac{\alpha}{2}\right)} \qquad (20)$$

with a significance level of $\alpha = 5\%$. We again expect (and are willing to accept) a model error of the fitted parametric distributions on top of the pure statistical noise considered by the standard KS-test. Therefore we subtract an extra 1% model error (chosen subjectively) from the value of KS_{test} before evaluating the test criterion. Hence, if a fitted curve passes this modified KS-test, the corresponding cumulative density function does not differ from the empirical one by more than 1% except for statistical noise.

3. Results and Discussion

3.1. Spatial Dependence of Distribution Shapes

[31] Per definition of our domain setup and MC scenarios, all statistics are invariant along the y-direction. In general, the z-direction will show less variation than the x-direction. This implies that, apart from their role in defining the mean flow direction, lateral boundaries are less influential on the space dependence of stochastic heads and velocities. In order to visualize the spatial dependence of the histograms along the x-direction, we plot empirical probability densities along the centerline of the domain. For a better overview of spatial dependence in all directions, we also plot empirical stochastic moments in space. In the following, we discuss these results for all variables of interest.

[32] Figures 1 and 2 show these plots (empirical probability densities and moments, respectively) for normalized hydraulic heads ϕ^*. The Dirichlet boundary conditions for head restrict the values of normalized head to a range between zero and unity. This causes the shape of its distribution to be similar to the beta distribution, where the mean exhibits the expected linear trend along the direction of mean flow. The variance is forced to zero at the boundaries because of the Dirichlet boundary condition
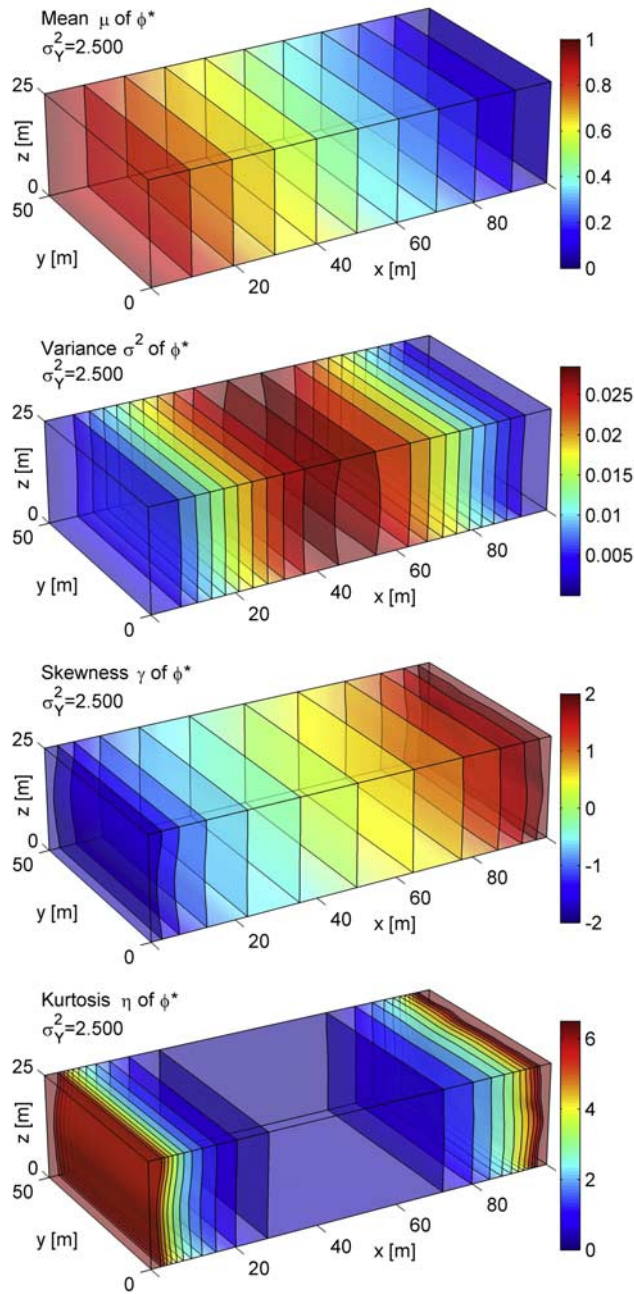
Figure 2. Empirical statistical moments (mean μ, variance σ^2, skewness γ and kurtosis η) of normalized hydraulic heads $\phi^* = \phi/\Delta\phi$ for MC scenario 6 ($\sigma_Y^2 = 2.5$). Left: averaged along the y-direction, right: prior to averaging.

and increases toward the center of the domain [e.g., *Zhang and Winter*, 1999]. The restriction of values to the interval of [0; 1] forces the distribution to be asymmetrical close to the boundaries, leading to a negative skewness near the inflow boundary and to a positive skewness near the outflow boundary. Close to the center of the domain, the distribution is almost Gaussian: the asymmetrical boundary influence vanishes if the distribution is far from the interval boundaries, so that both skewness and kurtosis approach values of zero. As a consequence, for smaller variances of log K, the region where a Gaussian distribution prevails and passes the corresponding fitting tests has a

larger extent than for larger variances. As an empirical rule of thumb based on this behavior, we suggest to trust the Gaussian shape at all locations in the domain where the bounding Dirichlet values are at least three standard deviations away from the mean value, i.e., when the 99% confidence interval of the assumed Gaussian is not cut off.

[33] The spatial dependence in the statistics of q_x^*, q_y^* and q_z^* is less pronounced by far (see Figure 3). The empirical pdf of the normalized longitudinal discharge component q_x^* is similar to a lognormal distribution with almost no spatial dependence along the x-axis. The empirical pdf for the normalized vertical discharge component q_z^* along the main direction of flow is shown in the bottom part of Figure 3. There seems to be no change in the distribution near the boundaries except for a smaller variance, which is caused by the prescribed pressure isosurface at the upstream and downstream boundaries. If we had evaluated velocities at nodes instead of at element centers, the variance would be exactly zero at $x = 0$ and $x = 100$. The distribution of q_y^* looks almost identical to that of q_z^* and is not shown here. The transverse components have conspicuously long and fat tails, which are not representable by a Gaussian distribution. The tails have been cut off in Figure 3. For example, q_y^* had
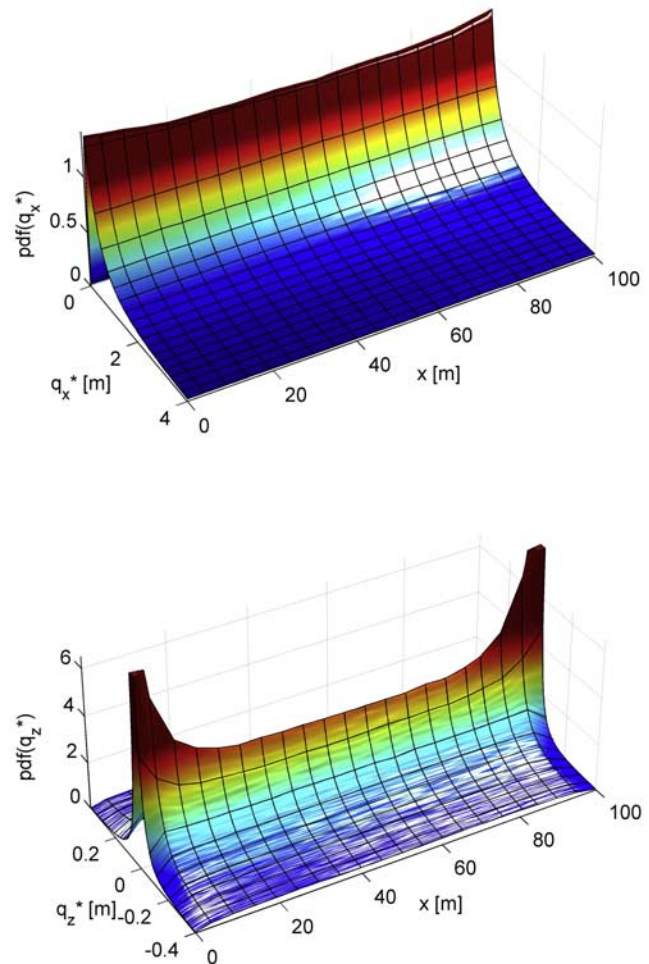
Figure 3. Evolution of the empirical probability densities of normalized longitudinal and transverse vertical discharge components $q_{x(z)}^* = q_{x(z)}/(K_e I_0)$ on the centerline along the main direction of flow for scenario 6 ($\sigma_Y^2 = 2.5$).
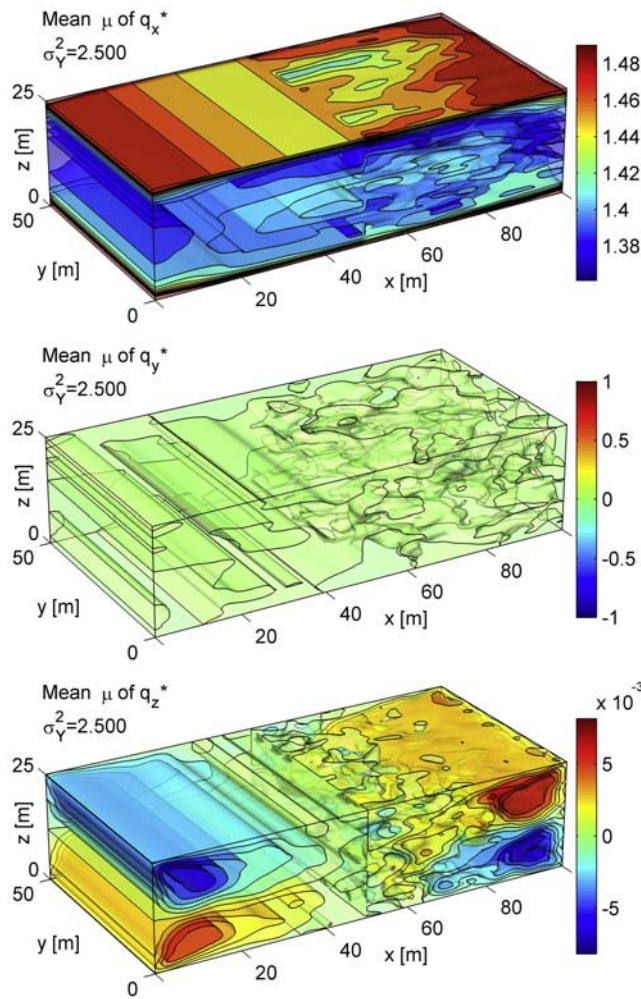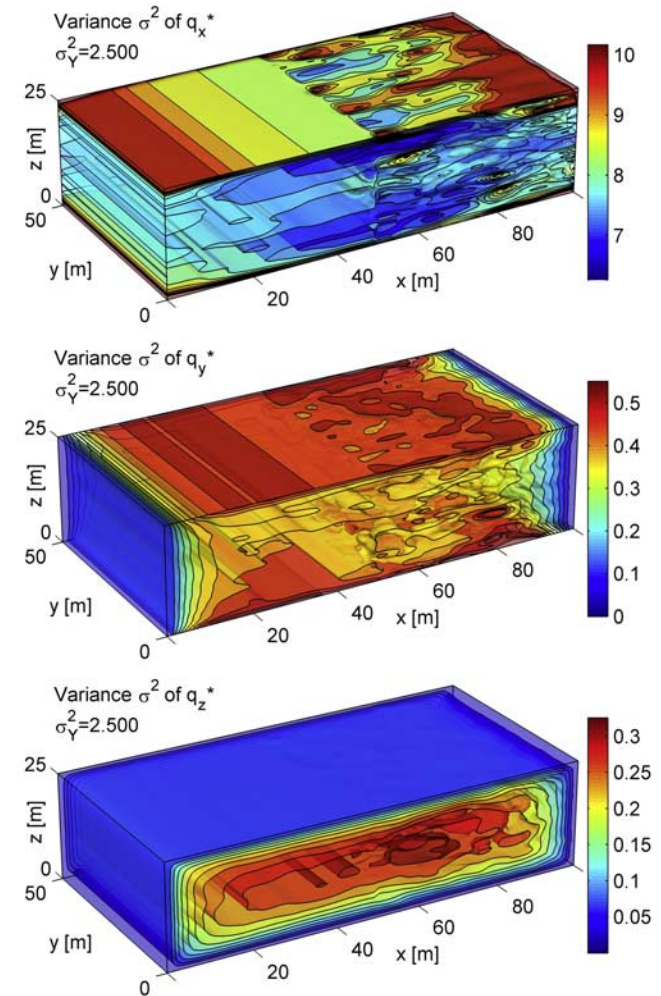
Figure 4. Empirical mean μ of normalized discharge components $q_i^* = q_i/(K_e I_0)$ for scenario 6 ($\sigma_Y^2 = 2.5$). Left: averaged along the y-direction, right: prior to averaging.

quantiles of $Q_{90\%} = 0.31$, $Q_{99\%} = 1.6$, $Q_{99.9\%} = 4.2$, $Q_{99.99\%} = 8.8$, and had its maximum observed value at $q_y^* = 117.7$.

[34] As a consequence of the lateral no-flow boundary conditions at the top and the bottom of the domain, there is a slight focusing of the mean z-component to the mid-level ($z = 0.5L_z$) of the domain, and a strong but thin focus area of the x-component along the top and bottom boundaries, as can be seen from Figure 4. The general pattern in the variance of discharge components (Figure 5) shows almost-zero variance of q_y^* and q_z^* at the upstream and downstream boundaries, almost-zero variance of q_z^* at the top and bottom no-flow boundaries. There is a corresponding increase of variances in q_x^* and q_y^* at the top and bottom of the domain because vertical discharge close to the no-flow boundaries is redirected into horizontal directions. As already discussed and demonstrated by many authors, the variances of the specific discharge components are influenced by the boundaries only in a region that is thinner than one correlation length [e.g., *Englert et al.*, 2006; *Rubin*, 2003; *Zhang*, 2002]. Higher-order features of the distributions of discharge components (not shown here) hardly depend on location, but depend heavily on the

variance of ln K, as discussed in the next section. Skewness and kurtosis are increasing toward the boundaries for all quantities. For discharge components, this happens within a region as thin as one correlation length, making the stochastic problem seemingly more non-linear within these regions.

[35] Figures 2, 4 and 5 show the moments averaged along the y-direction in the left halves of the domain, and prior to averaging in the right halves. The distributions of ϕ^* are very well-behaved with a relatively small variance compared to their spatial trends (especially close to the Dirichlet boundaries); hence their moments are virtually free of noise before averaging. This is entirely different for the moments of discharge components: Because of the fat and long tails of their distributions and their relatively large variational coefficients, the impact of few but very extreme realizations on the statistics is substantial (increasing with order of the moments), and $n_r = 25,000$ is insufficient to obtain satisfactory moments prior to averaging. Only after averaging along the y-direction are the mean and variance sufficiently free of noise to our satisfaction. The higher-order moments of discharge components, especially those of the transverse ones, are noisy even after this averaging and yield robust values only for larger volume averages including the other

Figure 5. Empirical variance σ^2 of normalized discharge components $q_i^* = q_i/(K_e I_0)$ for scenario 6 ($\sigma_Y^2 = 2.5$). Left: averaged along the y-direction, right: prior to averaging.
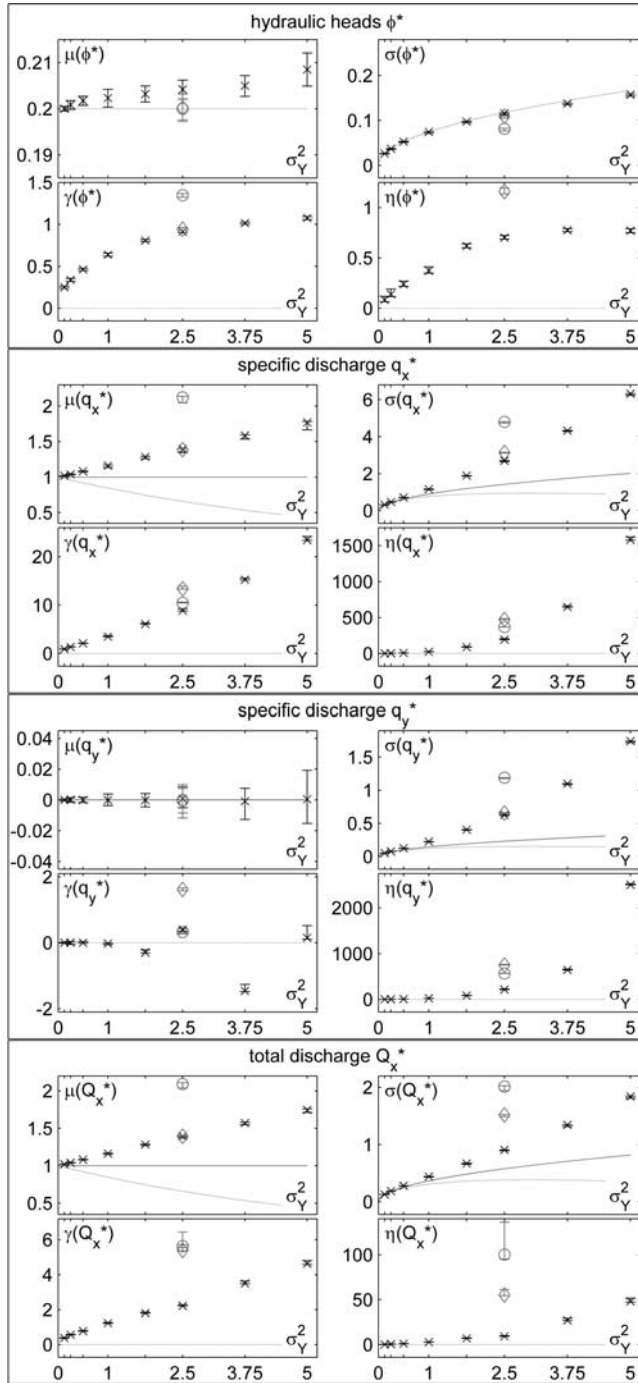
Figure 6. Dependence of empirical mean values μ_s, standard deviation σ_s, skewness γ_s and kurtosis η_s on σ_Y^2 for heads ϕ^* (off-center), specific discharge q_x^* (center of domain) and specific discharge q_y^* (center of domain) and total discharge Q_x^*. X marks, black: empirical values with 95% confidence intervals for multi-Gaussian fields (MC scenarios 1–8). Diamonds, gray: for high-K inclusions ($Y_{(+)}$, MC 9). Circles, gray: for low-K inclusions ($Y_{(-)}$, MC 10). Dotted black line: FOSM predictions. Solid gray line: FOSM scaled with $\exp(\sigma_Y^2/6)$.

dimensions. The degree of convergence of our MC analysis for stochastic moments is shown in Figure 6 as 95% confidence intervals. The values and confidence intervals in Figure 6 have been computed for point values of ϕ^* and for volume averages of q_i^* averaged over a pseudo-stationary volume taking 1/8 of the domain, as also in the articles by *Dykaar and Kitanidis* [1992] and *Englert et al.* [2006]. For fully resolved three-dimensional moments or instationary covariances between flow variables in bounded domains, we must recommend vastly higher numbers of realizations.

3.2. Dependence of Distribution Shapes on the Variance of log K

[36] The shapes of the empirical distributions depend heavily on the variance σ_Y^2 of log conductivity. Figure 7 shows a set of empirical distributions at specific locations for σ_Y^2 differing in the range from $\sigma_Y^2 = 0.125$ to $\sigma_Y^2 = 5$. It also shows maximum-likelihood fitted parametric distributions. The parametric distributions are chosen to honor physical restrictions like non-negativity or two-sided boundedness.

[37] For hydraulic heads ϕ^*, we show results at the location $(x, y, z) = (0.8L_x, 0.5L_y, 0.5L_z)$ in Figure 7 (top). This position, being off-center in the x-direction, evidently demonstrates how the boundedness of admissible values for ϕ^* is becoming increasingly important with increasing σ_Y^2, inducing an asymmetrical distribution as head fluctuations approach the restricting boundary value. The gradual change from a Gaussian distribution to a highly skewed one is quite obvious. Since the Dirichlet boundary conditions lead to the same effect near the outflow boundary, we hypothesize a behavior similar to the beta-distribution (see Table 2). The corresponding maximum-likelihood fit of beta distributions to the set of empirical distributions is shown as solid lines, revealing an almost suspiciously tight fit. Neither the χ^2 test according to equation (17) nor the KS test according to equation (19) rejected this hypothesis for any of the tested curves shown here. Small-variance cases with Gaussian distributions are covered by the beta distribution since it asymptotically approaches the Gaussian for $\sigma_s^2 \rightarrow 0$. Only in regions close to the boundary (not shown here) at high variances ($\sigma_Y^2 \geq 2.5$) was the fitted beta distribution rejected by both tests.

[38] For a variance of 1/12 and a mean value of 0.5, the beta-distribution is identical to the uniform distribution on [0; 1]. This is the limiting case for unimodal distributions (with mean value of one half) of all distributions bounded between zero and unity. Higher values inevitably lead to bimodal distributions, regardless of the actual distribution shape. Hence values of $\sigma^2(\phi^*) > 1/12$ at the domain center with $\mu(\phi^*) = 0.5$ will lead to bimodal distributions of ϕ^*. Such a high variance of ϕ^*, however, did not appear within the observed range of σ_Y^2. We assume that the limiting case for $\sigma_Y^2 \rightarrow \infty$ between two Dirichlet boundaries is the uniform distribution for heads.

[39] The statistics of all components of discharge do not vary over the largest part of the domain. Hence we discuss the location in the center of the domain. The longitudinal component q_x^* of the specific discharge (Figure 7, upper middle) is non-negative, if high-contrast structures in conductivity do not lead to a local reversal of flow. In our MC analysis, we could not observe negative values of q_x^* for any
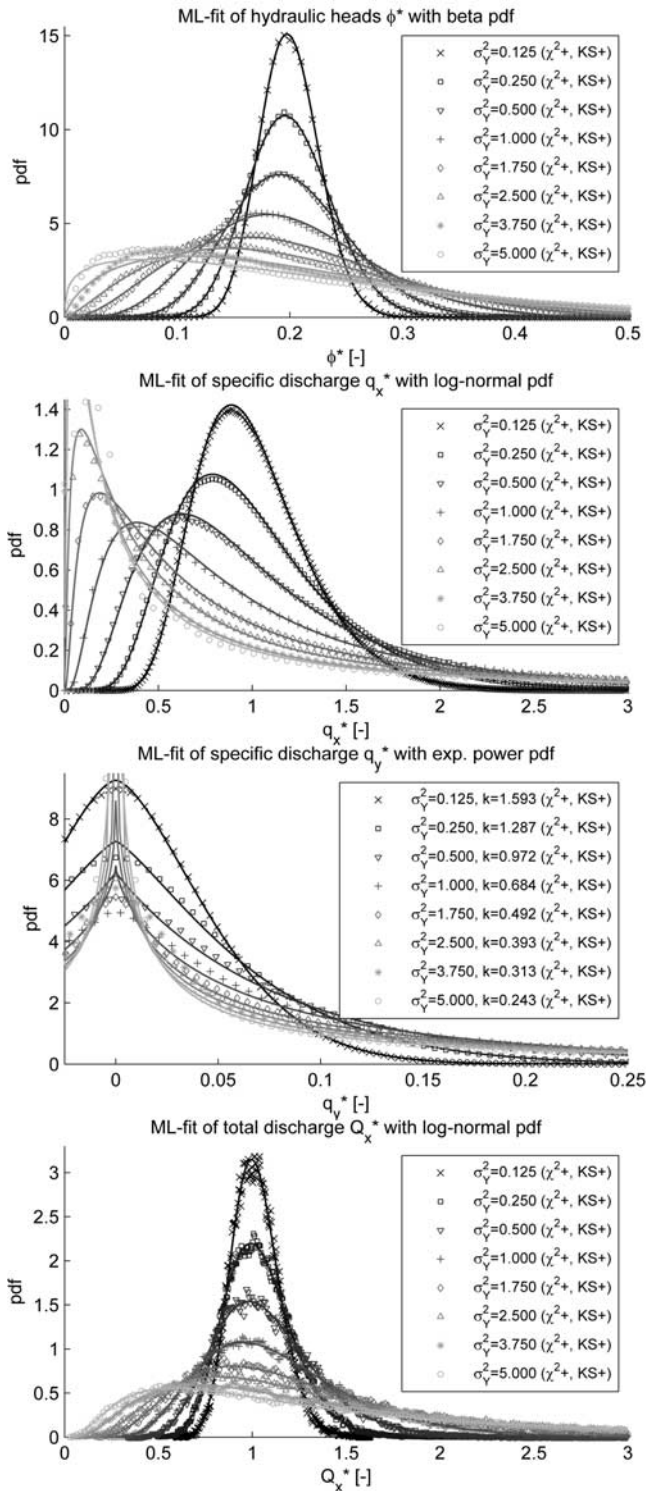
Figure 7. Maximum-likelihood fit of parametric distributions (solid lines) to the empirical distribution (marks) for heads ϕ^* (off-center), specific discharge q_x^* (center of domain) and specific discharge q_y^* (center of domain, symmetric about $q_y^* = 0$) and total discharge Q_x^* in MC scenarios with different σ_Y^2.

value of σ_Y^2 to any significant extent (see more detailed discussion below). This restriction to nonnegative values leads to skewed distributions for higher values of σ_Y^2. Hypothesizing and fitting the lognormal distribution is only

natural, and the ML-fitted lognormal distributions in Figure 7 match very well. The assumption of lognormal longitudinal velocities has already been used in the literature as an assumption, for example, in solute flux studies by *Dagan et al.* [1992] and *Cvetkovic et al.* [1992].

[40] For small-variance cases, one expects a Gaussian distribution of q_x^*. These cases are also covered by the lognormal distribution since it approaches the Gaussian for $\sigma_s^2/\mu_s^2 \rightarrow 0$. High-variance cases reveal a tendency to a heavier tailing behavior than the lognormal distribution (outside the plotted scale), but still no fitted curves were rejected anywhere in the domain. Surprisingly enough, the skewness is clearly visible and significant even for the case of $\sigma_Y^2 = 0.125$. One must conclude that a quasi-linear relation between perturbations of log conductivity and perturbations of discharge holds only for very low values of σ_Y^2, apparently still smaller than the minimum value of $\sigma_Y^2 = 0.125$ considered in this study. Hence a lognormal distribution should be used for q_x for all values of σ_Y^2.

[41] *Vanderborght et al.* [1998] have found an additional tailing behavior of longitudinal velocities toward smaller values in a study on solute flux in unsaturated heterogeneous soil. In their study, this tailing became apparent when plotting the log-velocity cdf in percentile-percentile plots with normal scale. They concluded that assuming lognormal distributions for q_x leads to an underrepresentation of almost-stagnant regions, affecting studies on solute flux. For variances of $\sigma_Y^2 \geq 3.75$, we occasionally observed reversal of flow at almost stagnant values of velocities in overall negligibly small areas of the domain. Other than that, we did not find evidence for excessive left tails of q_x in saturated media in the cases investigated in our study. *Englert et al.* [2006] have reported locally reversed flow in a Monte Carlo study in saturated heterogeneous media above $\sigma_Y^2 = 3$ and list several past studies which have found similar phenomena. They explain local flow reversal by tortuous S-shaped high-conductivity regions. This phenomenon was more significant in their study probably because they used larger, more ergodic domains where the forcing influence of the boundary conditions was more remote than in our study.

[42] Figure 7 (lower middle) shows the distribution of q_y^*. It also represents the transverse component q_z^* which hardly differs from this one in its distribution shape. Both distributions are symmetric about zero because the admissible range of values is not restricted and the domain setup is symmetric along the y and z planes. However, the nonlinearity of the stochastic problem leads to extremely heavy tailing for higher σ_Y^2. Apparently, a parametric distribution with an additional shape parameter is required, allowing to control the heaviness of tailing. We found the exponential power family (see Table 2) a suitable candidate. The corresponding ML-fitted exponential power distributions show sufficient agreement to not fail the χ^2-test and the KS-test, although it is obvious that just one shape parameter is insufficient to closely match the empirical distributions. The exponential power family again includes the Gaussian as special case for $k = 2$ and is more peaked (i.e., has a positive kurtosis and hence longer tails) for $k < 2$. For higher variance, the fitted curves get close to the pass/fail limit, which is mostly because of their inadequately pronounced peak at $s = 0$. However, the tailing behavior is reproduced

nicely. Since the statistics of q_y^* and q_z^* hardly change within our domain, no fitted curves in the entire domain were rejected.

[43] Figure 7 (bottom) shows the distribution of total discharge Q_x^*. The histogram is more noisy than that of q_x^* since the averaging of statistics over the periodic y-direction does not apply here. The fact that Q_x^* has a non-zero variance is a consequence of the bounded and non-ergodic domain. Thanks to the central limit theorem, however, its distribution is tighter and more Gaussian than that of q_x^*. For the same reasons as for q_x^*, we fit a lognormal distribution. The resulting curves showed an extremely good agreement and were not rejected for any value of σ_Y^2.

3.3. Deviations From Linear Stochastic Theory With Variance of ln K

[44] In order to quantify the deviations from linear stochastic theory, we visualize descriptive parameters of the empirical distributions as a function of σ_Y^2 in Figure 6. These are the mean, standard deviation (instead of variance for better plot scaling), skewness and kurtosis observed at the same locations as the histograms discussed above. Here the non-linearity of the flow problem is manifested in two phenomena: first, the gradual transition of the empirical distributions from Gaussian to other shapes. For Gaussian distributions, the skewness γ and kurtosis η are always zero, so that any non-zero value indicates a non-Gaussian distribution. Second, there are deviations of the empirical mean and variance from the values predicted by linear stochastic theory, here represented by our FOSM analysis.

[45] Hydraulic head ϕ^* at $(x, y, z) = (0.8L_x, 0.5L_y, 0.5L_z)$, shown in Figure 6 (top) convey a clear picture: the mean value changes a bit with increasing σ_Y^2. This change is related to a higher hydraulic gradient within a relaxation layer up to about one correlation length away from the boundary. It is statistically significant, but otherwise mostly negligible. The variance of heads increases slightly but significantly less than linearly with σ_Y^2, but the deviation from linear stochastic theory seem to be irrelevant up to $\sigma_Y^2 = 2.5$. Because of the off-center position at $x = 0.8L_x$, the skewness rises with increasing σ_Y^2, like it was to be expected from Figure 7 (top). For kurtosis, there are two superimposed competing effects: for non-central positions, kurtosis rises as the bounding value imposed by the closer boundary produces a distinct tail toward adverse values. For rather broad distributions, the bounding values imposed by both Dirichlet boundary conditions take effect and restrict both tails, enforcing a less peaked and rather uniform distribution with a decreasing kurtosis. In rather central positions, only the latter effect prevails, leading to strictly negative values. At the non-central position shown here, the first effect leads to the initial increase of kurtosis, while the second one leads to an attenuation of kurtosis for high values of σ_Y^2. If a consistent way to describe the skewness and kurtosis effects can be found that is satisfied with the mean and variance as input information, we hypothesize that using the mean and variance from FOSM analysis is sufficient to fully describe the distribution of heads. This hypothesis will be investigated in the next section.

[46] The moments of q_x^* in Figure 6 (upper middle) show two main effects: First, the mean grows faster than predicted by the effective hydraulic conductivity for infinite isotropic media, $K_e = \exp(\bar{Y} + \sigma_Y^2/6)$ (solid gray line). This phenom-

enon is no surprise: (1) there is an increased probability of continuous highly permeable paths connecting the inflow to the outflow boundary in bounded domains, and (2) anisotropy aligned with the direction of mean flow increases the effective conductivity even in infinite domains. Generalizations to anisotropic and bounded domains have been developed [e.g., *Paleologos et al.*, 1996] and agree with the effect observed here. Likewise, the boundedness of the domain increases the variance of q_x^* more than expected. This consequence, however, has not been quantified in analytical expressions in the literature up-to-date. The second effect shown by the moments of q_x^* is that the pronounced asymmetry and the extreme upper tailing strongly increase with σ_Y^2. This clearly demonstrates that the Gaussian distribution is inadequate for the longitudinal component of specific discharge.

[47] Q_x^* shows a quite similar behavior as q_x^*: the mean has the exact same increase with σ_Y^2. The dependence of σ_Q, skewness and kurtosis on σ_Y^2 is the same as that of q_x^* but for apparent factors of roughly 1/4, 1/5 and 1/50 (given our specific geometry and degree of non-ergodicity), respectively. We attribute this tendency to a more Gaussian distribution with a smaller variance to the fact that Q_x^* is the spatial average of q_x over Ω and the central limit theorem. For more ergodic domains, we observed an even more Gaussian shape with even smaller variance. At the ergodic limit, the variance is known to vanish. The even-order moments of transverse discharge components (here: q_y^*) are almost identical to those of q_x^*, but symmetry sets the odd moments (mean and skewness) to zero.

[48] Altogether, first-order theory performs quite poor for discharge, especially for $\sigma_Y^2 > 0.5$, but deviations from Gaussianity are apparent even at $\sigma_Y^2 = 0.125$. When using low-order approximations of discharge in conjunction with Gaussian distributions (e.g., in the context of risk assessment, for assessing solute mass fluxes or for evaluating dispersivities in heterogeneous porous media), the heavy tails and the inaccuracy of first-order mean values and variances imply that higher-order statistics (including higher-order moments) of transport processes and the reliability of first-order approaches for larger values of σ_Y^2 need to be investigated further. Quite interestingly, *Bellin et al.* [1992] found that different errors in linearizing flow and transport compensate for each other so that dispersivities derived from linear theory are sufficiently accurate even up to $\sigma_Y^2 = 1.6$.

3.4. Using First-Order Second-Moment Approximations

[49] In order to asses the utility of FOSM-based moments, we employ the method of moment matching in conjunction with the parametric distributions used above. For hydraulic heads, Figure 8 (top) illustrates that combining FOSM with the intuitively chosen beta distribution delivers surprisingly good results. Only in the high-variance cases with $\sigma_Y^2 \geq 2.5$ are the moment-matched curves rejected. This rejection is mainly because of the inexact behavior at the lower bounding value which originates from a slightly too high value for the variance. If we had used the Gaussian distribution instead, the results would have been a lot less encouraging: only up to $\sigma_Y^2 = 0.25$ is the skewness of the empirical distribution sufficiently small to fit with a Gaussian one.
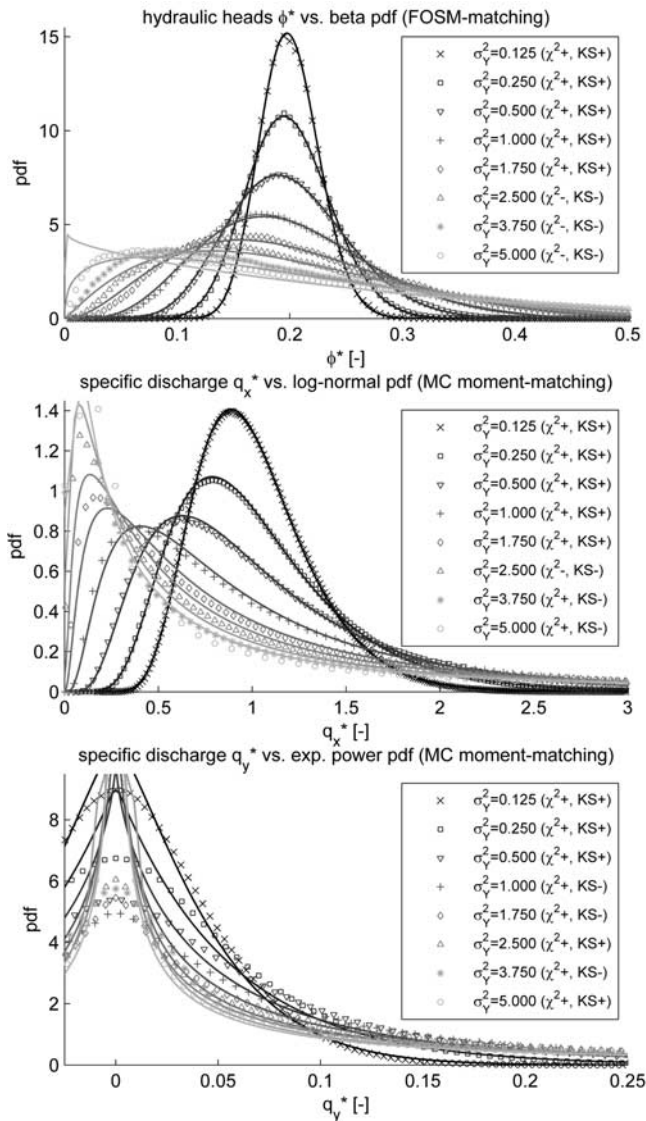
Figure 8. Comparison of parametric distributions obtained from moment matching, using moments from first-order second-moment or Monte Carlo analysis (solid lines) versus empirical distributions for head ϕ^* and discharge components q_x^* and q_y^* in MC scenarios with different σ_Y^2 (marks).

[50] For discharge components, the picture is less cheery. It is obvious from Figure 6 and the related discussion that the Gaussian shape will be a poor approximation in almost any case, and that FOSM-based moments are quite frustratingly poor. All curve fitting attempts based on FOSM moments, regardless of using the Gaussian or other parametric distributions, failed in the χ^2- and the KS-test. Since the lognormal distribution q_x^* and Q_x^* has been shown to be a reliable model for the pdf shape, higher-order accurate values for mean and variance are sufficient. The exponential power distribution for q_y^* and q_z^* requires at least a variance and a kurtosis (assuming the mean value to be zero) in order to be fitted, calling out for higher-order stochastic moments.

[51] Hence, instead of matching with FOSM moments, we demonstrate the advantage of having higher-order moments or higher-order expressions for mean and variance available by using our MC-based moments. Figure 8 (mid-

dle) shows the lognormal distribution for q_x^* with MC-based values for the mean and variance. All χ^2-tests pass but the for case of $\sigma_Y^2 = 2.5$. This single misfit seems to be an effect of statistical noise for the curves close to the pass/fail limit for high values of σ_Y^2. The KS-test fails only for high variances $\sigma_Y^2 \geq 2.5$. Higher-order analytical expressions for the mean and variance of longitudinal velocities are available and have been tested by *Englert et al.* [2006] in a Monte Carlo study.

[52] The comparison of curves from the exponential power family with empirical distributions for the transverse discharge components is shown in Figure 8 (bottom), based on MC-based values of the variance and kurtosis. The misfit of the pronounced peak at $q_y^* = 0$ is a rather local phenomenon, whereas the tails are fitting well over a large range. None of them was rejected by the χ^2 test, but some were just above the pass/fail limit in the KS-test due to their extreme peak at $q_y^* = 0$. Unfortunately, we could not find analytical expressions for higher-order moments of flow variables in the literature.

3.5. Special Cases

[53] Up to here, the generated random conductivity fields were multi-Gaussian. The non-linear transformation of Gaussian fields according to equation (6) leads to (1) inclusions of high-conductivity material (denoted by $Y_{(+)}$) with a connected low-permeable background or to (2) inclusions of low-conductivity material (denoted by $Y_{(-)}$) embedded in a connected highly permeable background (used in MC scenarios 9 and 10, respectively). Connectivity of extreme materials is known to lead to cumbersome effects in solute transport or in variably saturated flow, as has been discussed by *Zinn and Harvey* [2003], *Neuweiler and Cirpka* [2005], and *Neuweiler and Vogel* [2007]. In Figure 9, we compare empirical distributions of heads and discharge for $Y_{(+)}$, $Y_{(-)}$ to those in plain multi-Gaussian fields for reference, each for $\sigma_Y^2 = 2.5$. A comparison of the statistical moments is included in Figure 6.

[54] We first discuss the effect of low-conductivity inclusions ($Y_{(-)}$) with a connected backbone of preferential flow paths. The latter term is borrowed from multiphase flow, but seems to be graphically descriptive for the resulting flow patterns. While "path" applies to 2D fields, where the connected regions form tortuous lines, the term "skin" is more appropriate for three-dimensional domains, where the connected material resides around the inclusions in skin-like layers. For sufficiently high σ_Y^2, the inclusions can be regarded as dead zones of essentially stagnant water.

[55] From looking at heads in Figure 9 (top), the backbone obviously has an equilibrating effect on pressure, since the heads are much more clustered about their mean value, spoiling the good fit of the beta-distribution. This is measurable in a decreased variance and an increased kurtosis in Figure 6. For q_x^*, hardly any effect is visible in Figure 9 (upper middle). An increased mean value and variance of q_x^* (see Figure 6) is caused by a heavier and longer tail of extremely high velocities, which is not within the scale of Figure 9. Given the structure of stagnant regions nerved with preferential flow skins, a higher variance and mean value was to be expected. With the ratio between skewness and variance changed, the lognormal distribution is rejected. For transverse directions, here represented by q_y^*, the flow following the tortuous backbones leads to in-
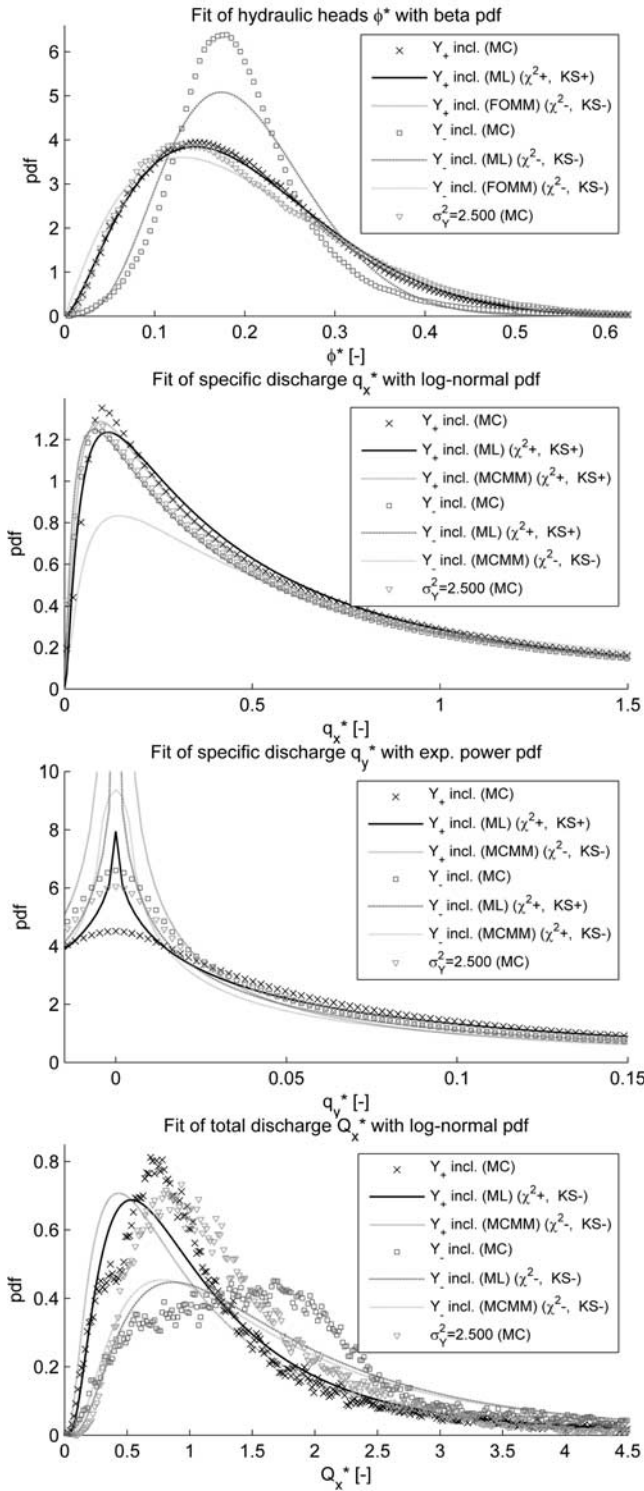
Figure 9. Maximum-likelihood (ML) fit of parametric distributions (solid and dash-dotted lines) to the empirical distribution (marks) for heads ϕ^* (off-center), specific discharge q_x^* (center of domain) and specific discharge q_y^* (center of domain) and total discharge Q_x^* in MC scenarios with different connectivity features for $\sigma_Y^2 = 2.5$. Marks: empirical distributions. Solid/dashed lines: ML fits. Dotted line: FOSM-based moment matching (FOMM, identical for all $Y_{(-)}$ and $Y_{(+)}$) or MC-based moment matching (MCMM, different for $Y_{(-)}$ and $Y_{(+)}$).

creased local deviations from the mean flow direction, increasing the variance through fatter and longer tails (again outside the scale of this plot). Because of the connectivity of high-conductivity paths, the total discharge Q_x^* also rises, the peakedness of the empirical shape is decreased, and the lognormal distribution is rejected. Altogether, the connected highly permeable material seems to adversely affect the fitting of the curves which matched well in the multi-Gaussian case.

[56] The case of high-conductivity inclusions $(Y_{(+)})$ leads to a connected network of low-permeably skins that try to prevent the high-permeable regions from participating in flow. Since the thickness of these skins is small, the highly permeable inclusions are still being flown through, and the effect of connectivity on the flow variables is less pronounced by far. As a matter of fact, the mean total discharge does not significantly differ from that for multi-Gaussian fields (see Figure 6), although one would intuitively expect a drastic decrease in effective conductivity. These findings are incompatible to recent findings for variably saturated flow [e.g., *Neuweiler and Cirpka*, 2005], where connected fine-material skins are those regions which maintain a higher saturation during drainage and form a flow-active network when coarse material is already close to residual saturation and hence almost impermeable. Altogether, the fitted curves are better than in the case of low-conductivity inclusions $(Y_{(-)})$. Especially the ML-fitting is successful in all cases, but the moment-matched distributions are rejected in all cases but for q_x^*.

[57] The remaining MC scenarios $11-13$ listed in Table 1 are not discussed in detail since they merely confirm expected phenomena:

[58] (1) If the Dirichlet inflow boundary is replaced by a Neumann boundary, hydraulic heads only have a one-sided bound. This makes them nonnegative but not restricted toward high values. The resulting hypothesized parametric distribution is the lognormal one. The lognormal distribution fits very well and is rejected nowhere in the domain.

[59] (2) For a linear covariance function (approximated by a spherical one with the range parameter h_r adjusted so that the range is at least two times the domain length in each direction), there is variability on all scales. The resulting fields are effectively less ergodic and the variance of all quantities rises, while the mean total discharge increases.

[60] (3) For smaller correlation length scales, keeping the domain size constant, the opposite effect applies.

4. Summary and Conclusions

[61] In this study, we have performed an extensive Monte Carlo analysis for hydraulic heads and discharge components in three-dimensional bounded and heterogeneous domains. The empirical probability distributions of heads and velocities are extremely non-Gaussian even for smaller variances of log conductivity. For the case of discharge, even $\sigma_Y^2 = 0.125$ lead to obviously different distribution shapes.

[62] By accounting for bounds of the distributions imposed by the boundary conditions of the flow problem, we intuitively found parametric distributions which fit the stochastic flow variables surprisingly well. For example, hydraulic heads without recharge obey the beta-distribution very well if they lie between two Dirichlet boundaries, and closely meet the lognormal distribution between a Dirichlet and a Neumann boundary. The longitudinal discharge component was

lognormal in all cases, and transverse components showed extremely heavy and long tailing, fitting the exponential power distribution with powers between 0.4 and 2. Using transformed fields with connectivity of highly permeable or hardly permeable material leads to more peculiar empirical distributions and heavily impaired the fitting.

[63] These findings let us judge the application of linear methods quite skeptically. In absence of better information, i.e., when only second moments are available or if the boundary conditions do not allow an intuitive choice of distributions that honor non-negativity or two-sided boundedness, the picture is quite poor. Especially the tailing behavior of transverse discharge components has the potential to affect studies on transverse dispersivities that assume multi-Gaussian distributions of velocities. Also, for the sake of risk assessment or stochastic design, distribution shapes need to be assumed in order to estimate exceedance probabilities. In absence of higher-order moments from higher-order accurate methods or knowledge of empirical distribution shapes, exceedance probabilities based on the assumption of Gaussianity will lead to highly erroneous results.

[64] We tested how good mean values and variances based on numerical first-order second-moment (FOSM) analysis are when using them in conjunction with the intuitively chosen parametric distributions that we found to fit the empirical ones. This analysis revealed that for hydraulic heads, FOSM-based moments are a powerful tool if used together with adequate parametric distributions. For the case of discharge components, FOSM-based moments performed too poorly for the moment-matching approach to succeed. Instead, we showed that higher-order accurate moments beyond the mean value and variance (here taken from our MC analysis) would suffice to obtain the same success for discharge components.

[65] In the case presented here, the simple geometry and boundary conditions offer a good support for choosing parametric distributions, and a few lower moments suffice to determine a well-fitting distribution. The main implication of this study is to use this intuitive but highly valuable information, if available. Unfortunately, information on non-negativity or two-sided boundedness will not always be available or applicable for complicated domain geometries with less trivial boundary conditions. Then, only direct evaluation of probability density functions or the conversion of higher-order moments to probability density functions [e.g., *Blinnikov and Moessner*, 1998] would help to avoid the application of brute-force Monte Carlo techniques. In the introduction, we have listed a number of studies that discuss higher-order accurate approaches to the stochastic flow problem. Ironically, although some of these methods can even be arbitrarily exact, none of the authors have implemented moments of orders higher than the variance.

[66] The second implication of this study is to further advance these methods toward higher-order moments or the direct evaluation of probability distributions, as has been done by *Li and Zhang* [2007]. When using Monte Carlo methods for higher-order moments of discharge in bounded domains (without exploiting ergodicity), numbers of realizations far above our $n_r = 25,000$ will have to be used because of the extremely long and fat tails of transverse discharge components. We expect, most of all, stochastic Galerkin methods to be offer a sufficiently flexible alterna-

tive tool in this context. The order of approximation, however, will have to be sufficiently high to meet at least the moments up to fourth order accurately.

Appendix A: Adjoint-State Sensitivities

[67] The evaluation of auto- and cross-covariances of dependent quantities in equations (14) and (15) require sensitivities as given by equation (13). We evaluate the sensitivities using the continuous adjoint-state method [e.g., *Sun*, 1994], linearized about the zeroth-order (homogeneous) solution $\bar{\phi}(\mathbf{x})$ using $\tilde{K}(\mathbf{x}) = K_g$. For each sensitivity, we solve one adjoint-state equation. The adjoint state $\psi_{\phi j}$ of ϕ observed at location $\mathbf{x}_j$ is [e.g., *Cirpka and Kitanidis*, 2001]:

$$-\nabla \cdot \left(\tilde{K}\nabla\psi_{\phi j}\right) = \delta\left(\mathbf{x}_j\right) \quad \text{in } \Omega$$

$$\mathbf{n} \cdot \left(\tilde{K}\nabla\psi_{\phi j}\right) = 0 \quad \text{on } \partial\Omega_{no} \qquad (A1)$$

$$\psi_{\phi j} = 0 \quad \text{on } \partial\Omega_D$$

where $\delta(\mathbf{x}_j)$ is the Dirac delta function at the location of observation. For specific discharge, adjoint-state sensitivities have not been reported in literature yet. For this study, we have developed a corresponding adjoint-state equation given by:

$$-\nabla \cdot \left(\tilde{K}\nabla\psi_{qij}\right) = \nabla \cdot \left(\mathbf{e}_i\delta(\mathbf{x}_j)\tilde{K}\right) \quad \text{in } \Omega$$

$$\mathbf{n} \cdot \left(\tilde{K}\nabla\psi_{qij}\right) = 0 \quad \text{on } \partial\Omega_{no} \qquad (A2)$$

$$\psi_{qij} = 0 \quad \text{on } \partial\Omega_D$$

where $\mathbf{e}_i$ is the unit vector in direction of the desired discharge component and

$$\nabla \cdot \left(\mathbf{e}_i\delta(\mathbf{x}_j)\right) = \frac{\partial}{\partial x_i}\delta\left(\mathbf{x}_j\right) \qquad (A3)$$

is a Dirac dipole at the location of observation. Weighted with $\tilde{K}$, this resembles the partial derivative of discharge with respect to heads. For the total discharge, we have developed an adjoint state ψ_{Qx} identical to the equation for ϕ with reversed Dirichlet boundary values:

$$-\nabla \cdot \left(\tilde{K}\nabla\psi_{Qx}\right) = 0 \quad \text{in } \Omega$$

$$\mathbf{n} \cdot \left(\tilde{K}\nabla\psi_{Qx}\right) = 0 \quad \text{on } \partial\Omega_{no} \qquad (A4)$$

$$\psi_{Qx} = -\hat{\phi} \quad \text{on } \partial\Omega_D$$

Given solutions to these adjoint-state equations (using the same numerical scheme as for the original governing equations), the sensitivities of a dependent variable s (ϕ, q_i and Q_x) observed at location $\mathbf{x}_j$ with respect to piecewise constant values Y_k within sub-volumes Ω_k (here: FEM grid cells with element center $\mathbf{x}_k$) are given by:

$$[\mathbf{H}_\phi]_{jk} = \frac{\partial\phi(\mathbf{x}_j)}{\partial Y_k} = -\int_{\Omega_k} \tilde{K}\left[\nabla\bar{\phi} \cdot \left(\nabla\psi_{\phi j}\right)\right] d\Omega,$$

$$[\mathbf{H}_{qi}]_{jk} = \frac{\partial q_i(\mathbf{x}_j)}{\partial Y_k} = -\int_{\Omega_k} \tilde{K}\left[\nabla\bar{\phi} \cdot \left(\nabla\psi_{qij} + \mathbf{e}_i\delta(\mathbf{x}_j)\right)\right] d\Omega \quad (A5)$$

$$[\mathbf{H}_{Qx}]_k = \frac{\partial Q_x}{\partial Y_k} = -\int_{\Omega_k} \tilde{K}\left[\nabla\bar{\phi} \cdot \left(\nabla\psi_{Qx}\right)\right] d\Omega$$

These integrals can be evaluated using analytical solutions of the element stiffness matrix (and related quantities) for all

sub-volumes Ω_k in one simultaneous third-order tensor multiplication [*Nowak*, 2005].

References

Abramowitz, M., and I. A. Stegun (1972), *Handbook of Mathematical Functions with Formulas, Graphs, and Mathematical Tables, 9th printing*, Dover, New York.

Bellin, A., P. Salandin, and A. Rinaldo (1992), Simulation of dispersion in heterogeneous porous formations: Statistics, first-order theories, convergence of computations, *Water Resour. Res.*, 28(9), 2211–2227.

Blinnikov, S., and R. Moessner (1998), Expansions for nearly Gaussian distributions, *Astron. Astrophys., Suppl. Ser.*, 130, 193–205.

Caroni, E., and V. Fiorotto (2005), Analysis of concentration as sampled in natural aquifers, *Trans. Porous Med.*, 59, 19–45, doi:10.107/s11242-004-1119-x.

Chaudhuri, A., and M. Sekhar (2005), Stochastic finite element method for the probabilistic analysis of flow and transport in a three-dimensional heterogeneous porous formation, *Water Resour. Res.*, 41, W09404, doi:10.1029/2004WR003844.

Cirpka, O. A., and P. K. Kitanidis (2001), Sensitivity of temporal moments calculated by the adjoint-state method, and joint inversing of head and tracer data, *Adv. Water Resour.*, 24(1), 89–103.

Cirpka, O. A., and W. Nowak (2004), First-order variance of travel time in non-stationary formations, *Water Resour. Res.*, 40, W03507, doi:10.1029/2003WR002851.

Cirpka, O. A., C. M. Bürger, W. Nowak, and M. Finkel (2004), Uncertainty and data worth analysis for the hydraulic design of funnel-and-gate systems in heterogeneous aquifers, *Water Resour. Res.*, 40, W11502, doi:10.1029/2004WR003352.

Cordes, C., and W. Kinzelbach (1992), Continuous groundwater velocity fields and path lines in linear, bilinear, and trilinear finite elements, *Water Resour. Res.*, 28(11), 2903–2911.

Cvetkovic, A., A. M. Shapiro, and G. Dagan (1992), A solute flux approach to transport in heterogeneous formations: 2. Uncertainty analysis, *Water Resour. Res.*, 28(5), 1377–1388, doi:10.1029/91WR03085.

Dagan, G., V. Cvetkovic, and A. M. Shapiro (1992), A solute flux approach to transport in heterogeneous formations: 1. The general framework, *Water Resour. Res.*, 28(5), 1369–1376.

Dentz, M., H. Kinzelbach, S. Attinger, and W. Kinzelbach (2002), Temporal behaviour of a solute cloud in a heterogeneous porous medium: 3. Numerical simulations, *Water Resour. Res.*, 38(7), 1118, doi:10.1029/2001WR000436.

Dentz, M., H. Kinzelbach, S. Attinger, and W. Kinzelbach (2003), Numerical studies of the transport behavior of a passive solute in a two-dimensional incompressible random flow field, *Phys. Rev. E*, 67(4), 046,306, doi:10.1103/PhysRevE.67.046306.

Dietrich, C. R., and G. N. Newsam (1993), A fast and exact method for multidimensional Gaussian stochastic simulations, *Water Resour. Res.*, 29(8), 2861–2869.

Dykaar, B. B., and P. K. Kitanidis (1992), Determination of the effective hydraulic conductivity for heterogeneous porous media using a numerical spectral approach: 1. Method, *Water Resour. Res.*, 28(4), 1155–1166.

Englert, A., J. Vanderborght, and H. Vereecken (2006), Prediction of velocity statistics in three-dimensional multi-Gaussian hydraulic conductivity fields, *Water Resour. Res.*, 42, W03418, doi:10.1029/2005WR004014.

Evans, M., N. Hastings, and B. Peacock (2000), *Statistical Distributions*, 3rd ed., John Wiley & Sons, Inc., New York.

Gelhar, L. W., and C. L. Axness (1983), Three-dimensional stochastic analysis of macrodispersion in aquifers, *Water Resour. Res.*, 19(1), 161–180.

Ghanem, R. (1998), Scales of fluctuation and the propagation of uncertainty in random porous media, *Water Resour. Res.*, 34(9), 2123–2136.

Guadagnini, A., and S. P. Neuman (1999), Nonlocal and localized analyses of conditional mean steady state flow in bounded, randomly nonuniform domains: 1. Theory and computational approach, *Water Resour. Res.*, 35(10), 2999–3018.

King, P. (1987), The use of field theoretic methods for the study of flow in a heterogeneous porous medium, *J. Phys. A*, 20, 3935–3947.

Kitanidis, P. K. (1997), *Introduction to Geostatistics*, Cambridge Univ. Press, Cambridge, U.K.

Law, A. M., and W. D. Kelton (1992), *Simulation modeling and analysis*, McGraw-Hill, New York.

Li, H., and D. Zhang (2007), Probabilistic collocation method for flow in porous media: Comparisons with other stochastic methods, *Water Resour. Res.*, 43, W09409, doi:10.1029/2006WR005673.

Lu, Z., and D. Zhang (2004), A comparative study on uncertainty quantification for flow in randomly heterogeneous media using Monte Carlo simulations and conventional and KL-based moment-equation approaches, *SIAM J. Sci. Comput.*, 26(2), 558–577.

Matthies, H. G., and A. Keese (2005), Galerkin methods for linear and nonlinear elliptic stochastic partial differential equations, *Comput. Methods Appl. Mech. Eng.*, 194(12–16), 1295–1331, doi:10.1016/j.cma.2004.05.027.

Naff, R. L., D. F. Haley, and E. A. Sudicky (1998), High-resolution Monte Carlo simulation of flow and conservative transport in heterogeneous porous media: 1. Methodology and flow results, *Water Resour. Res.*, 34(4), 663–676.

Neuman, S. P., S. Orr, O. Levin, and E. Paleologos (1992), Theory and high-resolution finite element analysis of 2-D and 3-D effective permeabilities in strongly heterogeneous porous media, in *Mathematical Modeling in Water Resources*, vol. 2, edited by T. F. Russel et al., pp. 118–136, Elsevier, New York.

Neuweiler, I., and O. A. Cirpka (2005), Homogenization of Richards equation in permeability fields with different connectivities, *Water Resour. Res.*, 41, W02009, doi:10.1029/2004WR003329.

Neuweiler, I., and H.-J. Vogel (2007), Upscaling for unsaturated flow for non-Gaussian heterogeneous porous media, *Water Resour. Res.*, 43, W03443, doi:10.1029/2005WR004771.

Nowak, W. (2005), Geostatistical methods for the identification of flow and transport parameters in subsurface flow, Ph.D. thesis, Institut für Wasserbau, Universität Stuttgart, http://elib.uni-stuttgart.de/opus/frontdoor.php?source_opus=2275.

Nowak, W., S. Tenkleve, and O. A. Cirpka (2003), Efficient computation of linearized cross-covariance and auto-covariance matrices of interdependent quantities, *Math. Geol.*, 35(1), 53–66.

Paleologos, E. K., S. P. Neuman, and D. Tartakovsky (1996), Effective hydraulic conductivity of bounded, strongly heterogeneous porous media, *Water Resour. Res.*, 32(5), 1333–1341.

Press, W. H., B. P. F. S. A. Teukolsky, and W. T. Vetterling (1992), *Numerical Recipes: The Art of Scientific Computing*, 2nd ed., Cambridge Univ. Press, Cambridge, U.K.

Rubin, Y. (2003), *Applied Stochastic Hydrogeology*, Oxford Univ. Press, Oxford, U.K.

Sun, N.-Z. (1994), *Inverse Problems in Groundwater Modeling, Theory and Applications of Transport in Porous Media*, Kluwer Academic Publishers, Dordrecht, Netherlands.

Vanderborght, J., D. Mallants, and J. Feyen (1998), Solute transport in a heterogeneous soil for boundary and initial conditions: Evaluation of first-order approximations, *Water Resour. Res.*, 34(12), 3255–3270.

Wonnacott, R. J., and T. H. Wonnacott (1990), *Introductory Statistics*, 5th ed., John Wiley, New York.

Xiu, D., and G. E. Karniadakis (2002), Modeling uncertainty in steady state diffusion problems via generalizd polynomial chaos, *Comput. Methods Appl. Mech. Eng.*, 191, 4927–4948.

Zhang, D. (2002), *Stochastic Methods for Flow in Porous Media*, Academic Press, San Diego, Calif.

Zhang, D., and Z. Lu (2004), An efficient, higher-order perturbation approach for flow in random porous media via Karhunen-Loève and polynomial expansions, *J. Comput. Phys.*, 194, 773–794.

Zhang, J., and C. L. Winter (1999), Moment equation approach to single-phase fluid flow in heterogeneous reservoirs, *Soc. Pet. Eng. J.*, 4(2), 118–127.

Zinn, B., and C. F. Harvey (2003), When good statistical models of aquifer heterogeneity go bad: A comparison of flow, dispersion, and mass transfer in connected and multivariate Gaussian hydraulic conductivity fields, *Water Resour. Res.*, 39(3), 1051, doi:10.1029/2001WR001146.

————————————

O. A. Cirpka and R. L. Schwede, Swiss Federal Institute of Aquatic Science and Technology (Eawag), Überlandstr. 133, 8600 Dübendorf, Switzerland. (olaf.cirpka@eawag.ch; ronnie.schwede@eawag.ch)

I. Neuweiler, Institute for Fluid Mechanics, Leibniz Universität Hannover, Appelstrasse 9a, 30167 Hannover, Germany. (neuweiler@hydromech.uni-hannover.de)

W. Nowak, Civil and Environmental Engineering, University of California at Berkeley, 760 Davis Hall, Berkeley, CA 94708-1710, USA. (wolfgang.nowak@berkeley.edu)